An Analytical Inversion of the Nonuniformly Attenuated Radon Transform With Variable Focal-Length Fan-Beam Collimators

Junhai Wen, *Member, IEEE*, Tianfang Li, *Student Member, IEEE*, and Zhengrong Liang, *Member, IEEE*

***Abstract*—Single photon emission computed tomography (SPECT) is based on the measurement of radiation emitted by a radiotracer injected into the patient. Because of photoelectric absorption and Compton scatter, the gamma photons are attenuated inside the body before arriving at the detector. A quantitative reconstruction must consider the attenuation, which is usually nonuniform. Novikov has derived an explicit inversion formula for the nonuniformly attenuated Radon transform for SPECT reconstruction of parallel-beam collimated projections. In this paper, we extend his research to variable focal-length fan-beam VFF collimator geometry. A ray-driven analytical formula for VFF reconstruction with nonuniform attenuation was derived. As a unified framework, this formula can be used for parallel-beam, fan-beam, and VFF collimators. Its accuracy is demonstrated by computer simulation experiments.**

***Index Terms*—Analytical SPECT reconstruction, nonuniform attenuation, variable focal length.**

I. Introduction

In single-photon emission computed tomography (SPECT), a radiopharmaceutical or radiotracer is injected intravenously into the patient and the radiotracer concentration distributions or uptake images within the body are reconstructed from the measurement of decayed gamma ray radiation, where the uptake images at a region of interest (ROI) directly reflect the cell function there. Because of photoelectric absorption and Compton scatter, the gamma photons are attenuated inside the body before arriving at the detector. Quantitative reconstruction of the radiotracer uptake images at any location inside the body requires accurate compensation for the attenuation.

In some cases, where the attenuation of the object can be assumed as uniform (for example in the human brain), Tretiak and Metz [1] developed an explicit inversion formula for the uniformly attenuated (or exponential) Radon transform in two dimensions for a parallel-beam collimator geometry. Their algorithm assumes that the attenuation coefficient is constant across the body. In the same time and later, Bellini *et al.* developed some alternative inversion algorithms [2]–[6]. More inversion algorithms were developed with extension to more complicated collimator geometries. For example, Weng *et al.* [7] extended the parallel-beam algorithm to a fan-beam collimator geometry by a coordinate transform. In their formula, a filter function is introduced, which is not a convolver as used in Tretiak and Metz's explicit inversion formula, but is a shift varying filter. Therefore, their algorithm has to filter the data point-by-point numerically, which requires intensive calculation time. You *et al.* [8], [9] derived a Cormack-type inversion of the exponential Radon transform by employing the circular harmonic transform directly in both projection space and image space, instead of Fourier space. It was applied to parallel-beam, fan-beam and variable focal-length fan-beam (VFF) collimator geometries. However, all of these algorithms are limited to uniform attenuation, which is not applicable for nonuniformly attenuating media, such as for cardiac studies, where a quantitative reconstruction must consider the nonuniform attenuation among the lungs, soft tissues, and ribs.

Much interest on analytical SPECT reconstruction with nonuniform attenuation and parallel-beam geometry has been seen in the last decade. Arbuzov *et al.* [10] presented an inversion of the attenuated Radon transform with nonuniform attenuation, but their result was not cast in the well-established filtered backprojection (FBP) form, which was later derived by Novikov [11]. In Novikov's work, an explicit inversion formula for the nonuniformly attenuated Radon transform for parallel-beam geometry is derived. This formula had been implemented and good reconstruction results were obtained [12]. Another version of the explicit inversion formula was later reported by Natterer [13], also for a parallel-beam geometry. For clinical applications, however, fan-beam and VFF collimators would be preferred for brain and chest imaging, respectively. Fan-beam collimation improves count density and spatial resolution for imaging small objects, but for cardiac studies, the fan-beam geometry encounters a truncation problem. VFF collimation overcomes this truncation problem, while preserving the improved count density and spatial resolution. In our previous work, we proposed an approximate reconstruction algorithm for fan-beam and VFF collimators and obtained very good reconstruction results [14]. An exact inversion formula for a fan-beam geometry was reported in [15]. In this work, we extend this exact ray-driven analytical reconstruction algorithm to a VFF collimator geometry.

The presentation of this work is organized as follows. In Sections II and III, we introduce basic notation and review previous reconstruction method for parallel-beam collimator geometry.

Manuscript received December 2, 2002; revised April 10, 2003. This work was supported in part by NIH National Heart, Lung, and Blood Institute under Grant HL54166.

J. Wen is with the Department of Radiology, State University of New York, Stony Brook, NY 11794 USA (e-mail: wenjh@mil.sunysb.edu).

T. Li is with the Departments of Physics and Radiology, State University of New York, Stony Brook, NY 11794 USA.

Z. Liang is with the Departments of Radiology and Computer Science, State University of New York, Stony Brook, NY 11794 USA.

Digital Object Identifier 10.1109/TNS.2003.817315

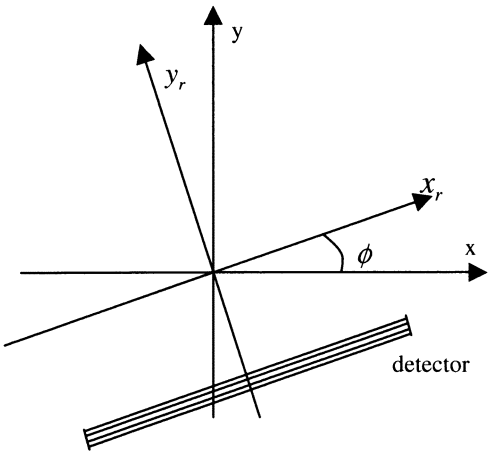

Fig. 1. The rotated coordinate system.

In Section IV, we derive our ray-driven analytical reconstruction algorithm for a VFF collimator geometry, based on our previous work for a fan-beam collimator geometry. In Section V, computer simulation results are presented to demonstrate the accuracy of the derived formulas. The discussion of the presented method and conclusions of the presented results are given in the last section.

II. Basic Notation

The notation of [12] will be used throughout this paper. In order to simplify the derivation, a rotated coordinate system (x_r, y_r) is introduced (see Fig. 1)

$$\begin{aligned} x_r &= x\cos\phi + y\sin\phi \\ y_r &= -x\sin\phi + y\cos\phi. \end{aligned} \tag{1}$$

Then the measured projection data at angle ϕ can be expressed as

$$g_\phi(x_r) = \int_{-\infty}^{\infty} \exp[-(D_\phi a_\phi)(x_r, y_r)] f_\phi(x_r, y_r)\, dy_r \tag{2}$$

where $f(x, y)$ denotes the activity source distribution to be reconstructed and $a(x, y)$ is the nonuniform attenuation coefficient across the body. Note that $g_\phi(x_r)$ is the projection datum at position x_r with projection angle ϕ. The divergent beam transform is

$$\begin{aligned} (D_\phi a_\phi)(x_r, y_r) &= D_\phi\{a_\phi(x_r, y_r)\} \\ &= \int_{y_r}^{detector} a_\phi(x_r, y_r')\, dy_r'. \end{aligned} \tag{3}$$

In SPECT, the gamma photons are attenuated before arriving at the detector, so $\exp[-(D_\phi a_\phi)(x_r, y_r)]$ is the attenuation of gamma photons emitted from point (x_r, y_r) before they arrive at the detector with angle of ϕ [16]–[18].

III. Reconstruction for Parallel-Beam Collimator

According to [11]–[13], the parallel-beam reconstruction formula can be written as follows:

$$f(x, y) = \frac{1}{4\pi}\int_0^{2\pi} \frac{\partial}{\partial x_r}\left(e^{(D_\phi a_\phi)(x_r, y_r)} g a_\phi(x_r)\right) d\phi \tag{4}$$

where

$$\begin{aligned} &g a_\phi(x_r) \\ &= e^{-A_\phi(x_r)}\Big[\cos(E_\phi(x_r)) H\Big\{\cos(E_\phi(x_r)) e^{A_\phi(x_r)} g_\phi(x_r)\Big\} \\ &\quad + \sin(E_\phi(x_r)) H\Big\{\sin(E_\phi(x_r)) e^{A_\phi(x_r)} g_\phi(x_r)\Big\}\Big] \end{aligned} \tag{5}$$

and

$$\begin{aligned} A_\phi(x_r) &= \tfrac{1}{2} R_\phi\{a_\phi(x_r, y_r)\} \\ E_\phi(x_r) &= H\{A_\phi(x_r)\}. \end{aligned} \tag{6}$$

Notation $R_\phi\{\cdot\}$ represents the Radon transform at angle ϕ

$$R_\phi\{a_\phi(x_r, y_r)\} = \int_{-\infty}^{\infty} a_\phi(x_r, y_r)\, dy_r \tag{7}$$

and $H\{\cdot\}$ denotes the Hilbert transform

$$H\{A(x)\} = \frac{1}{\pi}\int_{-\infty}^{\infty} \frac{A(t)}{x - t}\, dt. \tag{8}$$

According to [11]–[13], (4) can also be written by the following formulas (which are more easily adapted by our ray-driven method)

$$f(x, y) = \frac{1}{4\pi}\left(\frac{\partial}{\partial x} B_C(x, y) + \frac{\partial}{\partial y} B_S(x, y)\right) \tag{9}$$

where

$$\begin{aligned} B_C(x, y) &= \int_0^{2\pi} \left[e^{(D_\phi a_\phi)(x_r, y_r)} g a_\phi(x_r)\right] \cos\phi\, d\phi \\ B_S(x, y) &= \int_0^{2\pi} \left[e^{(D_\phi a_\phi)(x_r, y_r)} g a_\phi(x_r)\right] \sin\phi\, d\phi \end{aligned} \tag{10}$$

and $g a_\phi(x_r)$ was defined by (5).

The parallel-beam reconstruction process can be described as follows.

a) Compute the divergent beam transform $D_\phi\{a_\phi(x_r, y_r)\}$ and the Radon transform $R_\phi\{a_\phi(x_r, y_r)\}$.
b) Calculate the modified projections $g a_\phi(x_r)$.
c) Backprojection with the weight for each point as shown by (10). With the different weights $\cos\phi$ and $\sin\phi$, two images $B_c(x, y)$ and $B_s(x, y)$ are obtained. ($B_c(x, y)$, $B_s(x, y)$) is a vector image.
d) Calculate the divergence of (9).

In order to formulate our ray-driven reconstruction method, we modify (5) as follows. Since

$$H\{A(x)\} = \frac{1}{\pi}\int_{-\infty}^{\infty} \frac{A(t)}{x - t}\, dt$$

so that

$$\begin{aligned} &H\left\{\cos(E_\phi(x_r)) e^{A_\phi(x_r)} g_\phi(x_r)\right\} \\ &= \int_{-\infty}^{\infty} \frac{1}{x_r - x_r''}\left(\cos(E_\phi(x_r'')) e^{A_\phi(x_r'')} g_\phi(x_r'')\right) dx_r'' \end{aligned} \tag{11}$$

$$\begin{aligned} &H\left\{\sin(E_\phi(x_r)) e^{A_\phi(x_r)} g_\phi(x_r)\right\} \\ &= \int_{-\infty}^{\infty} \frac{1}{x_r - x_r''}\left(\sin(E_\phi(x_r'')) e^{A_\phi(x_r'')} g_\phi(x_r'')\right) dx_r'' \end{aligned} \tag{12}$$

where x_r'' is an integral variable, indicating the location of a ray. By substituting (11) and (12) into (5), we have

$$\begin{aligned} ga_\phi(x_r) = e^{-A_\phi(x_r)} \Bigg[& \cos(E_\phi(x_r)) \int_{-\infty}^{\infty} \frac{1}{x_r - x_r''} \\ & \cdot \left(\cos(E_\phi(x_r'')) e^{A_\phi(x_r'')} g_\phi(x_r'') \right) dx_r'' \\ & + \sin(E_\phi(x_r)) \int_{-\infty}^{\infty} \frac{1}{x_r - x_r''} \\ & \cdot \left(\sin(E_\phi(x_r'')) e^{A_\phi(x_r'')} g_\phi(x_r'') \right) dx_r'' \Bigg]. \end{aligned} \quad (13)$$

Because $A_\phi(x_r)$ and $E_\phi(x_r)$ are constant at position x_r, (13) can be rewritten as

$$\begin{aligned} & ga_\phi(x_r) \\ & = \int_{-\infty}^{\infty} e^{-A_\phi(x_r)} \Bigg[\cos(E_\phi(x_r)) \\ & \quad \cdot \left(\cos(E_\phi(x_r'')) e^{A_\phi(x_r'')} g_\phi(x_r'') \right) \frac{1}{x_r - x_r''} + \sin(E_\phi(x_r)) \\ & \quad \cdot \left(\sin(E_\phi(x_r'')) e^{A_\phi(x_r'')} g_\phi(x_r'') \right) \frac{1}{x_r - x_r''} \Bigg] dx_r'' \\ & = \int_{-\infty}^{\infty} ga_{(\phi, x_r'')}(x_r)\, dx_r'' \end{aligned} \quad (14)$$

where

$$\begin{aligned} & ga_{(\phi, x_r'')}(x_r) \\ & = e^{-A_\phi(x_r)} \Bigg[\cos(E_\phi(x_r)) \Bigg(\cos(E_\phi(x_r'')) \\ & \quad \cdot e^{A_\phi(x_r'')} g_\phi(x_r'') \frac{1}{x_r - x_r''} \Bigg) + \sin(E_\phi(x_r)) \\ & \quad \cdot \left(\sin(E_\phi(x_r'')) e^{A_\phi(x_r'')} g_\phi(x_r'') \frac{1}{x_r - x_r''} \right) \Bigg] \end{aligned} \quad (15)$$

$ga_{(\phi, x_r'')}(x_r)$ can be seen as the reconstruction contribution of ray (ϕ, x_r'') at projection position x_r, and $ga_\phi(x_r)$ is the reconstruction contribution of all rays with view angle ϕ at projection position x_r.

Substituting (14) into (10), (9) and (10) can be rewritten as

$$f(x, y) = \frac{1}{4\pi} \left(\frac{\partial}{\partial x} B_C(x, y) + \frac{\partial}{\partial y} B_S(x, y) \right) \quad (16)$$

and

$$\begin{aligned} & B_C(x, y) \\ & = \int_0^{2\pi} \int_{-\infty}^{\infty} \left[e^{(D_\phi a_\phi)(x_r, y_r)} ga_{(\phi, x_r'')}(x_r) \right] \cos\phi\, dx_r''\, d\phi \\ & B_S(x, y) \\ & = \int_0^{2\pi} \int_{-\infty}^{\infty} \left[e^{(D_\phi a_\phi)(x_r, y_r)} ga_{(\phi, x_r'')}(x_r) \right] \sin\phi\, dx_r''\, d\phi \end{aligned} \quad (17)$$

where $ga_{(\phi, x_r'')}(x_r)$ was defined by (15).

Equations (16) and (17) are our parallel-beam ray-driven reconstruction formulas. Based on these formulas, we will derive our VFF ray-driven reconstruction formulas in the next section. In order to facilitate the derivation, we present the following formulas.

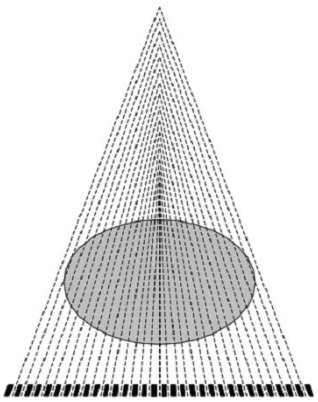

Fig. 2. Variable focal-length fan-beam collimator system.

According to the property of δ-functions, we know,

$$\begin{aligned} & H\left\{ \cos(E_\phi(x_r'')) e^{A_\phi(x_r'')} g_\phi(x_r'') \delta(x_r - x_r'') \right\} \\ & \quad = \cos(E_\phi(x_r'')) e^{A_\phi(x_r'')} g_\phi(x_r'') \frac{1}{x_r - x_r''} \\ & H\left\{ \sin(E_\phi(x_r'')) e^{A_\phi(x_r'')} g_\phi(x_r'') \delta(x_r - x_r'') \right\} \\ & \quad = \sin(E_\phi(x_r'')) e^{A_\phi(x_r'')} g_\phi(x_r'') \frac{1}{x_r - x_r''}. \end{aligned} \quad (18)$$

So (15) can be rewritten as

$$\begin{aligned} & ga_{(\phi, x_r'')}(x_r) \\ & = e^{-A_\phi(x_r)} \Big[\cos(E_\phi(x_r)) H\Big\{ \cos(E_\phi(x_r'')) e^{A_\phi(x_r'')} \\ & \quad \cdot g_\phi(x_r'') \delta(x_r - x_r'') \Big\} + \sin(E_\phi(x_r)) H \\ & \quad \cdot \Big\{ \sin(E_\phi(x_r'')) e^{A_\phi(x_r'')} g_\phi(x_r'') \delta(x_r - x_r'') \Big\} \Big]. \end{aligned} \quad (19)$$

Thus, we can use discrete Hilbert transform formula to calculate the value $ga_{(\phi, x_r'')}(x_r)$ of (15).

IV. Reconstruction for Variable Focal-Length Fan-Beam Collimator

In a VFF collimator system, the focal length varies according to the distance from the collimator to the center of the system [19]–[21]. Fig. 2 shows the VFF collimator system.

Any ray (p, β) in the VFF geometry can be seen as a ray (x_r, ϕ) in parallel-beam geometry (see Fig. 3 below). Let $D(p)$ be the variable focal length function. The relation between the parallel-beam and VFF geometries is

$$\begin{aligned} \phi &= \beta + \gamma = \beta + \arctan \frac{p}{D(p)} \\ x_r &= p\cos\gamma = \frac{pD(p)}{\sqrt{D(p)^2 + p^2}}. \end{aligned} \quad (20)$$

For each ray (p, β), we can build a local coordinate system (u, v) (see Fig. 4). The relation between this local coordinate system and the original coordinate system is

$$\begin{aligned} u &= x\cos\phi + y\sin\phi \\ v &= -x\sin\phi + y\cos\phi. \end{aligned} \quad (21)$$

In this local coordinate system, ray (p, β) will be a parallel-beam ray. So we can use our parallel-beam ray-driven

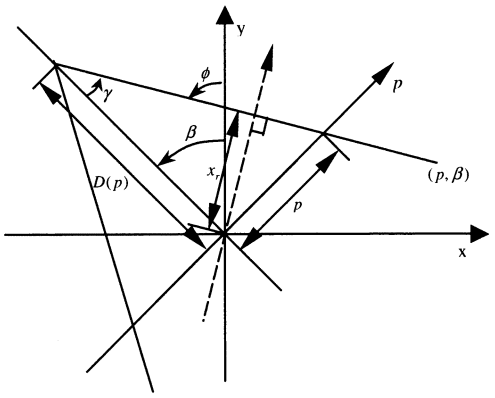

Fig. 3. The relation between parallel-beam and VFF geometries.

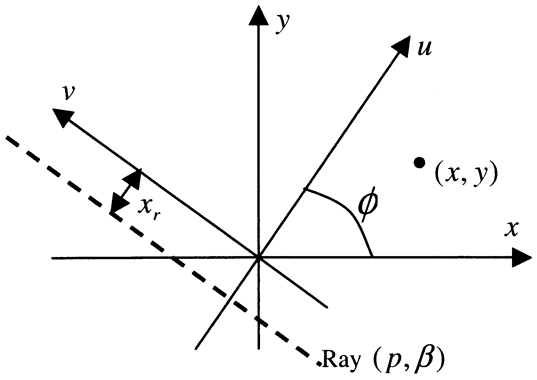

Fig. 4. The local coordinate system.

reconstruction formula to calculate the reconstruction contribution of this ray for every reconstruction point. For any point (x, y), its position in this local coordinate system is (u, v).

The coordinate system transform between the parallel-beam and VFF systems is associated with the relation of the change in differentials

$$dx_r\, d\phi = |J|\, dp\, d\beta \tag{22}$$

where the Jacobian $|J|$ is given by

$$|J| = \begin{vmatrix} \partial x_r/\partial p & \partial x_r/\partial \beta \\ \partial \phi/\partial p & \partial \phi/\partial \beta \end{vmatrix} = \frac{D^3(p) + p^3 D'(p)}{\sqrt{(D^2(p) + p^2)^3}}. \tag{23}$$

Our ray-driven analytical VFF reconstruction formula can be written as

$$f(x, y) = \frac{1}{4\pi}\left(\frac{\partial}{\partial x} B_C(x, y) + \frac{\partial}{\partial y} B_S(x, y)\right) \tag{24}$$

$$B_C(x, y) = \int_0^{2\pi}\int_{-\infty}^{\infty}\left[e^{(D_\phi a_\phi)(u, v)} g a_{(\beta, p)}(u)\right] \cdot \cos\phi |J|\, dp\, d\beta$$

$$B_S(x, y) = \int_0^{2\pi}\int_{-\infty}^{\infty}\left[e^{(D_\phi a_\phi)(u, v)} g a_{(\beta, p)}(u)\right] \cdot \sin\phi |J|\, dp\, d\beta \tag{25}$$

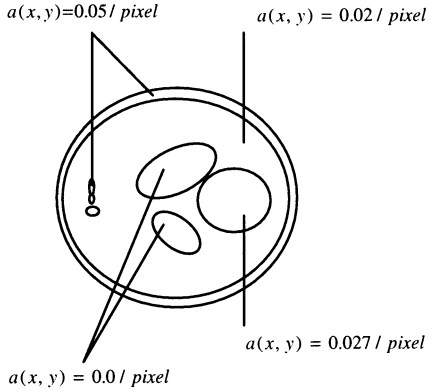

Fig. 5. Attenuation coefficients in the attenuation map of Fig. 6.

where

$$ga_{(\beta, p)}(u) = e^{-A_\phi(u)}\Big[\cos(E_\phi(u))H\Big\{\cos(E_\phi(x_r))e^{A_\phi(x_r)} \cdot g(p, \beta)\delta(u - x_r)\Big\} + \sin(E_\phi(u))H \cdot \Big\{\sin(E_\phi(x_r))e^{A_\phi(x_r)} g(p, \beta)\delta(u - x_r)\Big\}\Big]$$

$$E_\phi(u) = H\{A_\phi(u)\}, \text{ and } A_\phi(u) = \tfrac{1}{2} R_\phi\{a_\phi(u, v)\}. \tag{26}$$

The relation between (x, y) and (u, v) is shown by (21). The relation between (p, β) and (x_r, ϕ) is shown by (20). Therefore, (u, v) can be obtained by (x, y), and (x_r, ϕ) can be obtained by (p, β).

Because x and y are original coordinates, (24) does not depend on the geometry, it is the same as (16). Any ray (p, β) in the VFF geometry can be seen as a ray (x_r, ϕ) in the parallel-beam geometry. In the local coordinate system (u, v), the VFF ray is a parallel-beam ray, and the position of this ray is given by (x_r, ϕ). Using (25) and (26), the reconstruction contribution of this ray to every reconstruction points is calculated and back-projected with corresponding weights. By using a ray-by-ray manner and after all VFF rays are considered, two images $B_c(x, y)$ and $B_s(x, y)$ are generated, where $[B_c(x, y), B_s(x, y)]$ is a vector image. By the use of (24), the reconstructed image is obtained.

In [13], an approximation to H is given by the following:

$$H_\Omega\{g(u)\} = v_\Omega(u) * g(u) \tag{27}$$

where

$$v_\Omega(u) = \frac{1}{2\pi} L(\Omega u), \qquad L(u) = (1 - \cos(u))/u \tag{28}$$

$\Omega > 0$ is the bandwidth, and $*$ means convolution. This formula was utilized to compute the discrete Hilbert transform in our computer simulations.

V. Simulations

Computer simulation studies were carried out to test the derived formulas using the Shepp–Logan mathematical phantom with nonuniform attenuation on an image array of 128 × 128 pixel size. Attenuation factors in the attenuation map are shown in Fig. 5. Fig. 6(a) and (b) show the activity distribution and the attenuation map.

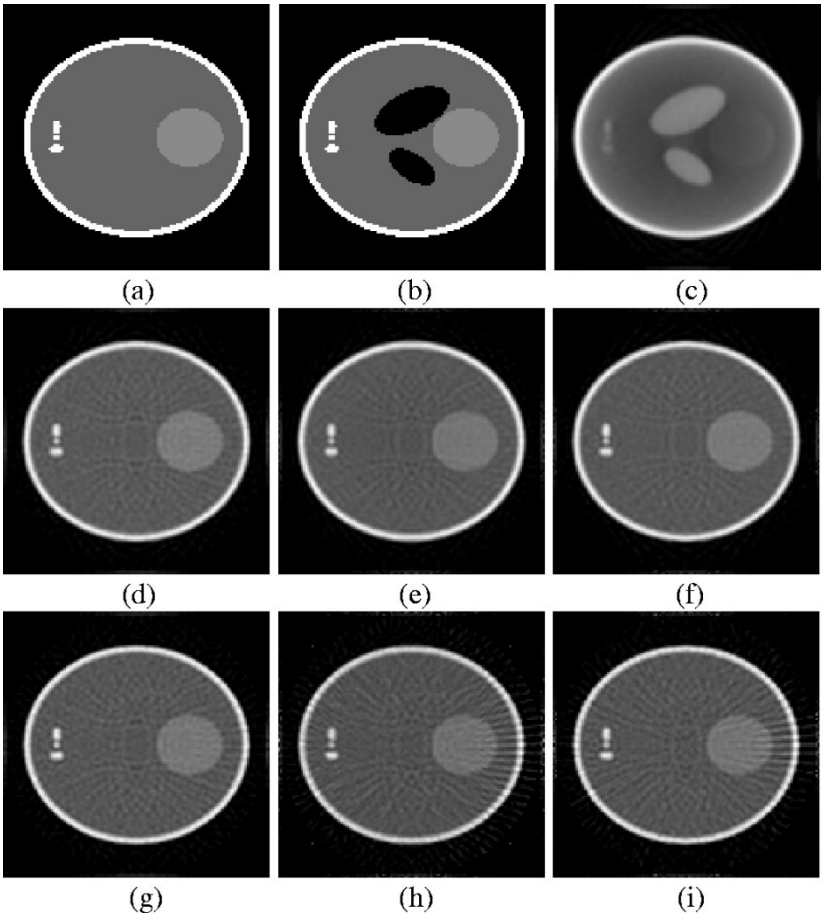

Fig. 6. Reconstruction results using our VFF algorithm, where $D(p)$ represents the focal length in pixel units, and the image size is 128 $\times$ 128. (a) Activity phantom. (b) Attenuation map. (c) FBP reconstruction of attenuated data without attenuation compensation. Simulations on (d), (e) and (f) did not consider attenuation for implementation test purpose. The reconstruction results of our VFF algorithm are: (d) for parallel-beam geometry by setting $D(p) = \infty$; (e) for fan beam geometry by setting $D(p) = 300$; and (f) for VFF geometry of $D(p) = 300 + 30|p|$. Simulations on (g), (h) and (i) studies considered the nonuniform attenuation. The reconstruction results of our VFF algorithm are: (g) for parallel-beam geometry by setting $D(p) = \infty$; (h) for fan beam geometry by setting $D(p) = 300$; and (i) for VFF geometry of $D(p) = 300 + 30|p|$.

For the parallel-beam geometry, 128 projections were simulated evenly spaced over 360 degrees by a circular orbit, each with 128 bins. For the fan-beam geometry, the focal length was chosen as $D(p) = 300$ in pixel units. Again, 128 projections were simulated evenly spaced over 360° by a circular orbit, each with 128 bins on the "detection plane" at the center of the FOV (field of view). For the VFF geometry, we tested two focal length functions of $D(p) = 200 + 10|p|$ and $D(p) = 300 + 30|p|$. For each focal length function, 128 projections were simulated evenly over a circular orbit, each with 128 bins on the "detection plane" at the center of the FOV.

Fig. 6(c) shows the conventional FBP reconstruction of the parallel-beam attenuated projections without compensation for the attenuation. A strong nonuniform attenuation artifact is clearly seen. Those projection rays which pass through the higher attenuation areas of the attenuation map will suffer more severe attenuation. Therefore, the reconstructed emission image at those higher attenuation areas becomes darker or has lower image densities than the expected values.

In order to verify the data simulation and processing procedures, we performed another test on the projection simulation and image reconstruction. By setting the attenuation coefficients to be zero, we simulated the nonattenuated projections of parallel-beam, fan-beam, and VFF collimators, respectively. The parallel-beam projections were reconstructed by our VFF algorithm with the focal length toward infinity and attenuation coefficients being zero. The result is shown in Fig. 6(d), which is almost identical to the result of the conventional FBP reconstruction [22]. With the focal length of our VFF algorithm fixed to the constant of 300 pixel units and attenuation coefficients being zero, the reconstruction of the fan-beam projections is shown in Fig. 6(e), which is almost identical to the result of the FBP fan-beam reconstruction [23]. The reconstruction of the VFF projections by our VFF algorithm is shown in Fig. 6(f), which is almost identical to the result of our previous reported harmonic decomposition method [8]. This test demonstrates the correct implementation of our VFF algorithm.

The reconstruction of the parallel-beam nonuniformly attenuated projections was performed by our VFF algorithm with its focal length toward infinity. The result is shown in Fig. 6(g), which is almost identical to the result of the parallel-bean nonuniform attenuation algorithm [11], [12]. The fan-beam attenuated projections were reconstructed by fixing the focal length for our VFF algorithm as a constant equal to that of the fan-beam collimator, i.e., 300 pixel units. The reconstructed image is shown in Fig. 6(h). The reconstructed image from the

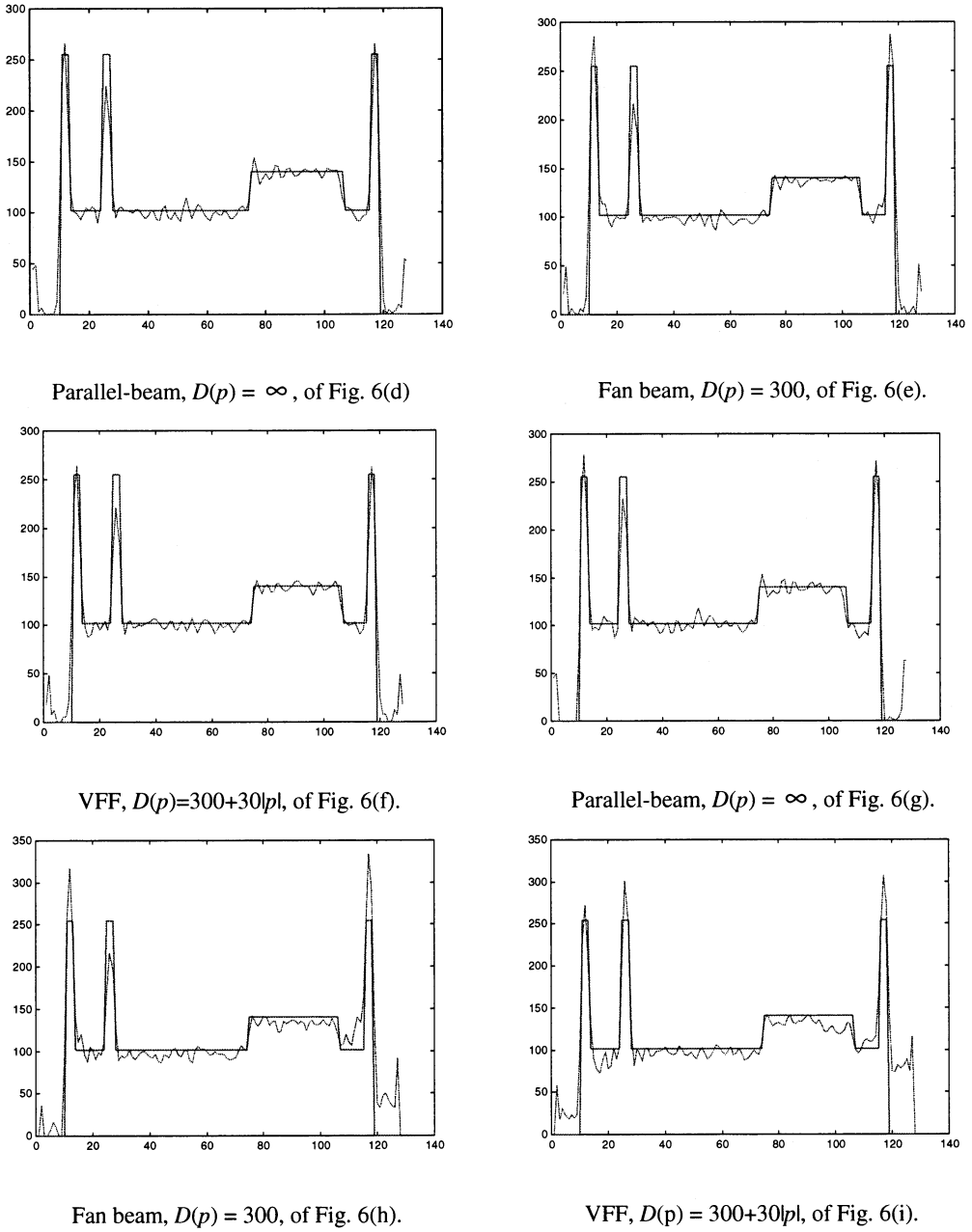

Fig. 7. Horizontal profiles of the reconstructed images (dotted lines) of Fig. 6 through the image center with comparison to the phantom profile (solid line).

VFF attenuated projections is shown in Fig. 6(i). These results are very similar, except for the strip artifacts near the edge of the FOV, which are also seen for the parallel-beam attenuation algorithm [11], [12] and will be discussed later.

Fig. 7 shows the horizontal profiles of the reconstructed images (dotted lines) of Fig. 6(d)–(i), and compares them with the profile of the phantom image (solid line). From this figure, it is seen that the profiles of the reconstructed images are very close to that of the phantom. The profiles of reconstructed images from nonattenuated projections are closer to the profile of the phantom image than those of reconstructed images from attenuated projections. The profiles of reconstructed images of parallel-beam projections are closer to the profile of the phantom image than those of reconstructed images of nonparallel beam projections. We also can see the strip artifacts near the edge of the FOV in the profiles of reconstructed images of fan-beam and VFF attenuated projections.

The phantom used in the above study is suitable for brain imaging. To show the algorithms' performance for chest imaging, another simulation was carried out using a chest activity phantom and attenuation map (see Fig. 8). Fig. 8(a) is the activity phantom. The attenuation coefficients in the three areas of the attenuation map of Fig. 8(b) are 0.027 (for the "bone"), 0.020 (for the "tissues") and 0.0 (for the "lungs") per pixel, respectively. The projections for parallel-beam, fan-beam and VFF collimators were simulated by the same

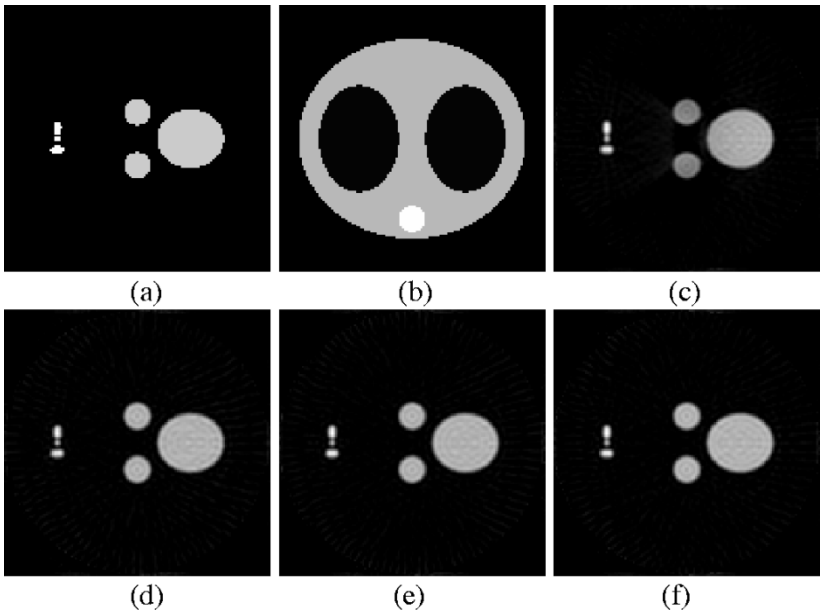

Fig. 8. Reconstruction results of our VFF algorithm for different conditions. $D(p)$ represents the focal length function in pixel units and the image size is 128 × 128. (a) Activity phantom. (b) Attenuation map. (c) Reconstruction without attenuation compensation. d) Parallel-beam $D(p) = \infty$. (e) VFF $D(p) = 200 + 10|p|$. (f) VFF $D(p) = 300 + 30|p|$.

protocol as described before. The parallel-beam data were first reconstructed by our VFF algorithm with the attenuation coefficients being zero and focal length toward infinity, and the result is shown in Fig. 8(c), which is almost identical to the conventional FBP reconstruction, where the strong artifact due to nonuniform attenuation is clearly seen again (i.e., the dark and deformation in the middle two circles and the nonuniformity across the large ellipse area).

With attenuation compensation, the reconstruction results using parallel-beam attenuated data is shown in Fig. 8(d), which is almost identical to the results for the parallel-beam nonuniform attenuation algorithm of Novikov [11], [12]. Two reconstructions for different focal length functions are shown in Fig. 8(e) and (f), respectively. These very similar results demonstrate the robustness of our VFF algorithm for different collimator geometries and the same performance of our algorithm and Novikov formula [4], [10] for the same parallel-beam geometry.

To compare our nonparallel beam algorithm for nonuniform attenuation compensation with currently available methods consisting of a rebinning technique (from nonparallel, e.g., fan-beam [24], to parallel-beam geometry) and Novikov's parallel-beam formula, we designed another phantom experiment, which involves a tiny point activity source embedded in a nonuniformly attenuating media (see Fig. 9). The attenuation map is the same as in the prior simulation experiment. Fig. 9(c) and (d) show the reconstructed results by the rebinning technique/parallel-beam formula and our VFF algorithm, respectively, (where the focal length was set as a constant for fan-beam geometry $D(p) = 150$ pixel units). Fig. 9(e) shows the profile of Fig. 9(c) along the horizontal line through the point source. Fig. 9(f) shows the profile of Fig. 9(d) along the same horizontal line as Fig. 9(e). Fig. 9(g) shows the profile of Fig. 9(c) along the vertical line through the point source. Fig. 9(h) shows the profile of Fig. 9(d) along the same vertical line as Fig. 9(g). It is obvious that the reconstructed point-source image by the rebinning technique and parallel-beam formula is blurred [the reconstructed point source is bigger than the original point, as clearly seen in Fig. 9(g)]. This is expected, since any rebinning will introduce some degrees of blurring. From these figures, we observed that the profiles of our VFF reconstructed image are very close to that of the phantom image; while the reconstructed image of the rebinning/parallel-beam formula is blurred and shows a noticeable variation from the phantom image.

VI. Discussions and Conclusion

From Figs. 6, 8, and 9, artifacts in the peripheral area of the reconstructed images are observed for results derived with parallel-beam, fan-beam and VFF collimators (the same observation for parallel-beam geometry is also reported in [12]). The artifacts in the VFF reconstruction are more obvious than those in the fan-beam reconstruction, and the artifacts in the fan-beam reconstruction are more obvious than those of parallel-beam reconstruction. Our algorithm is based on a ray-driven strategy, i.e., for a ray, its projection is a point. This requires that the involved discrete Hilbert transform has a wide bandwidth with a smooth property in the spatial domain. Fig. 10 shows the discrete Hilbert transform that was used in our VFF algorithm. According to (27) and (28)

$$\begin{aligned} H(0) &= 0.0 \\ H(n) &= (1 - \cos(n \cdot bandwidth))/(n \cdot bandwidth) \\ & \qquad n = 1, 2, \ldots, 127 \\ H(128) &= 0.0 \\ H(n) &= -H(256 - n), \qquad n = 129, 130, \ldots 255 \\ bandwidth &= 2.0, \text{ it is an experiential value.} \end{aligned}$$

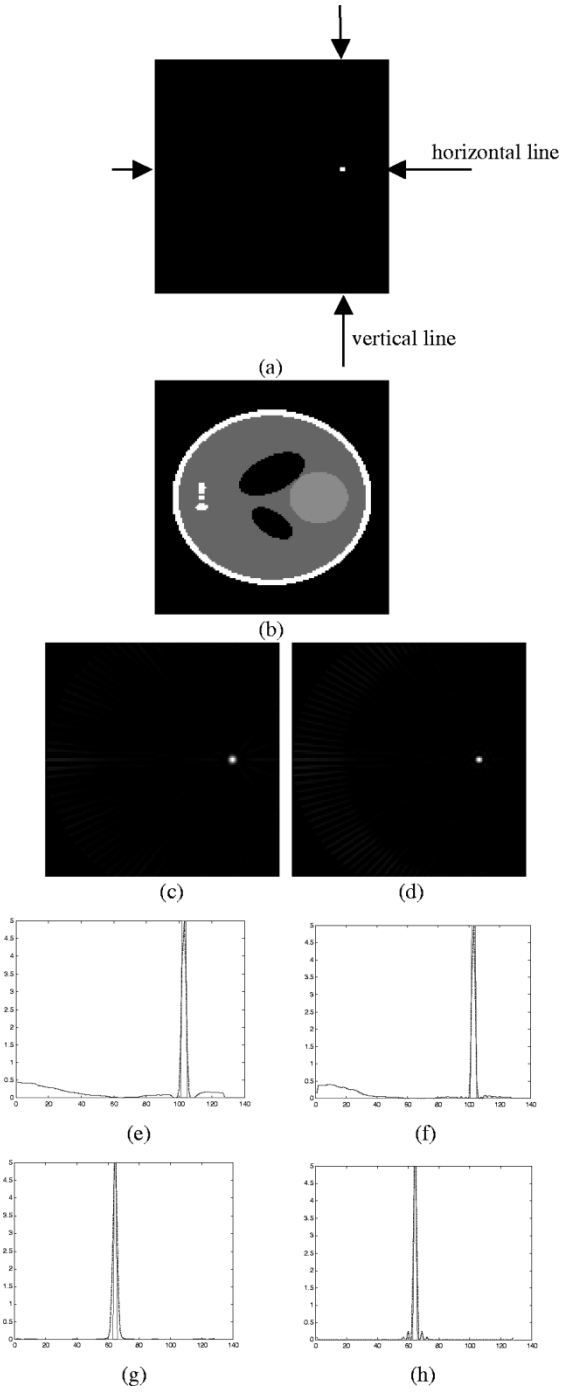

Fig. 9. (a) Activity phantom (a point). (b) Attenuation map. (c) Reconstructed image using the rebinning technique and parallel-beam formula. (d) Reconstructed image using our VFF algorithm. (e) Profile of Fig. 8(c) along the horizontal line. (f) Profile of Fig. 8(d) along the same horizontal line. (g) Profile of Fig. 8(c) along the vertical line. (h) Profile of Fig. 8(d) along the same vertical line.

It has a wide bandwidth, but does not have a smooth property in the spatial domain. This is the main cause for interpolation errors, leading to the more obvious artifacts than that of the parallel-beam algorithm of Novokov [11], [12]. Therefore, two tasks are currently being pursued. One is to investigate the cause of artifacts in the simple parallel-beam geometry. The other is to modulate the Hilbert transform for a minimal interpolation error.

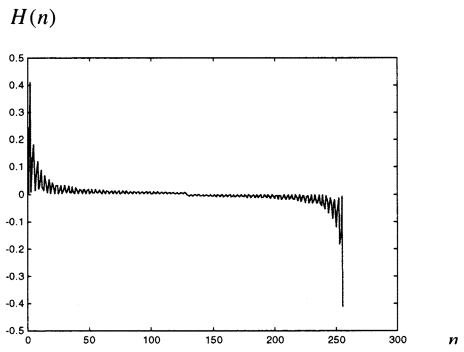

Fig. 10. Discrete Hilbert transform that we use in this paper.

In conclusion, we have derived a ray-driven analytical inversion algorithm for the nonuniformly attenuated Radon transform for a VFF geometry, based on the Jacobian relation between two different coordinate transformations. It is theoretically attractive because of its applicability to VFF, fan-beam and parallel-beam collimators. The computer simulation experiments have demonstrated its accuracy and robustness for different collimator geometries. Its noise properties and integration with scatter compensation and detector resolution correction are currently under investigation [25]–[27].

REFERENCES

[1] O. J. Tretiak and C. E. Meta, "The exponential Radon transform," *SIAM J. Appl. Math.*, vol. 39, pp. 341–354, 1980.

[2] S. Bellini, M. Piacentini, C. Cafforio, and F. Rocca, "Compensation of tissue absorption in emission tomography," *IEEE Trans. Acoust. Speech Signal Processing*, vol. ASSP-27, pp. 213–218, 1979.

[3] G. T. Gullberg and T. F. Budinger, "The use of filtering methods to compensate for constant attenuation in single photon emission computed tomography," *IEEE Trans. Biomed. Eng.*, vol. BME-28, pp. 142–157, 1981.

[4] T. Inouye, Y. Kose, and A. Hasegawa, "Image reconstruction algorithm for single photon emission computed tomography with uniform attenuation," *Phys. Med. Biol.*, vol. 34, pp. 299–304, 1989.

[5] W. G. Hawkins, P. K. Leichner, and N. C. Yang, "The circular harmonic transform for SPECT reconstruction and boundary condition on the Fourier transform of the sinogram," *IEEE Trans. Med. Imaging*, vol. 7, pp. 135–148, 1988.

[6] C. E. Metz and X. Pan, "A unified analysis of exact methods of inverting the 2-D exponential Radon transform with implications for noise control in SPECT," *IEEE Trans. Med. Imaging*, vol. 17, pp. 643–658, 1995.

[7] Y. Weng, L. Zeng, and G. T. Gullberg, "Analytical inversion formula for uniformly attenuated fan-beam projections," *IEEE Trans. Nucl. Sci.*, vol. 44, pp. 243–249, 1997.

[8] J. You, Z. Liang, and G. L. Zeng, "A unified reconstruction framework for both parallel-beam and variable focal-length fan-beam collimators by a Cormack-type inversion of exponential Radon transform," *IEEE Trans. Med. Imaging*, vol. 18, pp. 59–65, 1999.

[9] J. You, Z. Liang, and S. Bao, "A harmonic decomposition reconstruction algorithm for spatially varying focal length collimators," *IEEE Trans. Med. Imaging*, vol. 17, pp. 995–1002, 1998.

[10] E. V. Arbuzov, A. L. Bukhgeim, and S. G. Kazantsev, "Two-dimensional tomography problems and the theory of A-analytic functions," *Siberian Adv. Math.*, vol. 8, pp. 1–20, 1998.

[11] R. Novikov, "An inversion formula for the attenuated X-ray transformation," (in preprint), , May 2000.

[12] L. Kunyansky, "A new SPECT reconstruction algorithm based on the Novikov's explicit inversion formula," *Inverse Problems*, vol. 17, pp. 293–306, 2001.

[13] F. Natterer, "Inversion of the attenuated Radon transform," *Inverse Problems*, vol. 17, pp. 113–119, 2001.

[14] J. Wen, T. Li, X. Li, and Z. Liang, "Fan-beam and variable-focal-length fan-beam SPECT reconstruction with nonuniform attenuation," *J. Nucl. Medicine Technol.*, vol. 30, p. 97, 2002.

[15] J. Wen, T. Li, and Z. Liang, "Ray-driven analytical fan-beam SPECT reconstruction with nonuniform attenuation," in *Proc. IEEE Int. Symp. Biomedical Imaging*, 2002, pp. 629–632.

[16] G. T. Gullberg, "The attenuated radon transform: Theory and application in medicine and biology," Ph.D. dissertation, Univ. California—Berkeley, Berkeley, CA, 1979.

[17] G. Han, "Image reconstruction in quantitative cardiac SPECT with varying focal-length fan-beam collimators," Ph.D. Dissertation, State Univ. New York, Stony Brook, NY, 2000.

[18] Z. Liang, J. Ye, J. Cheng, and D. Harrington, *Quantitative Brain SPECT in Three Dimensions: An Analytical Approach to Non-Uniform Attenuation Without Transmission Scans*, ser. Computat. Imaging Vision. Norwell, MA: Kluwer, 1996, pp. 117–132.

[19] J. You, S. Bao, and Z. Liang, "Benefits of angular expression to reconstruction algorithms for collimators with spatially varying focal length," *IEEE Trans. Med. Imaging*, vol. 16, pp. 527–531, 1997.

[20] G. L. Zeng, G. T. Gullberg, R. J. Jaszczak, and J. Li, "Fan-beam reconstruction algorithm for a spatially varying focal length collimator," *IEEE Trans. Med. Imaging*, vol. 12, pp. 575–582, 1993.

[21] G. L. Zeng and G. T. Gullberg, "A backprojection filtering algorithm for a spatially varying focal length collimator," *IEEE Trans. Med. Imaging*, vol. 13, pp. 549–556, 1994.

[22] L. Shepp and B. Logan, "The Fourier reconstruction of a head section," *IEEE Trans. Nucl. Sci.*, vol. NS-21, pp. 21–43, 1974.

[23] R. Huesman, G. Gullberg, W. Greenberg, and T. Budinger, *Donner Algorithms for Reconstruction Tomography*. Berkeley, CA: Lawrence Berkeley Lab., Univ. California—Berkeley, 1977.

[24] T. Zhuang, *Principle and Algorithm of CT*. Shanghai, China: Shanghai Jiaotong Univ., 1992.

[25] T. Li, J. Wen, and Z. Liang, "Compensation for nonstationary detector response in analytical varying focal-length fan-beam SPECT reconstruction," in *Proc. IEEE NSS MIC Conf. Rec. (CD-ROM)*, 2002.

[26] X. Li, G. Han, H. Lu, L. Li, and Z. Liang, "A new scatter estimation method using triple window acquisition to fit energy spectrum," *J. Nucl. Medicine*, vol. 42, p. 194, 2001.

[27] H. Lu, J. Wen, X. Li, T. Li, G. Han, and Z. Liang, "Toward analytical solution for 3D SPECT reconstruction with nonuniform attenuation and distance-dependent resolution variation: A Monte Carlo simulation study," *SPIE Medical Imaging*, vol. 4684, pp. 20–28, 2002.